THE ASTRONOMICAL JOURNAL, 119:2118–2133, 2000 May

E+A GALAXIES IN THE NEAR-INFRARED: BROADBAND PHOTOMETRY

GASPAR GALAZ[1]
Las Campanas Observatory, Observatories of the Carnegie Institution of Washington, Casilla 601, La Serena, Chile; gaspar@azul.lco.cl
Received 1999 August 10; accepted 2000 February 10

ABSTRACT

This paper presents near-IR photometry of a selected sample of southern hemisphere E+A galaxies. The sample includes 50 galaxies from nearby ($z \sim 0.05$) and distant ($z \sim 0.3$) clusters, as well as E+A galaxies from the field ($z \sim 0.1$). Observations include 13 normal early-type galaxies from the field and from clusters to be compared with the E+A sample. The photometry includes J, H, and K_s apparent magnitudes and colors. Observed colors are obtained from the apparent total magnitudes and compared with those of the GISSEL96 spectrophotometric models of galaxy evolution. There is an overall agreement between integrated colors of models and observed ones, for both the E+A galaxies located in clusters and those in the field, at $z \lesssim 0.1$. However, large differences between colors predicted from models and those observed in E+A galaxies located in clusters at $z \sim 0.3$ are found. We also compute rest-frame colors for all the galaxies using two different sets of K-corrections and obtain average colors for all the samples. This work investigates systematic properties of the E+A sample as a function of its environment. Results seem to indicate that cluster E+A galaxies (at low redshift) are bluer than field E+A galaxies at $z \sim 0.1$. Even this conclusion does not depend on whether we use comoving or rest-frame colors or on the models used to obtain rest-frame colors; the difference is not significant enough, considering color dispersions between the samples. If the differences are real, they could imply a different stellar content for the E+A galaxies located in the field compared with those located in the cluster E+A galaxies.

Key words: galaxies: fundamental parameters — galaxies: photometry — galaxies: stellar content

1. INTRODUCTION

The attention drawn to E+A (or poststarburst) galaxies has increased since it was claimed that their fraction observed in clusters is correlated with the Butcher-Oemler effect (Butcher & Oemler 1978; Dressler & Gunn 1983; Rakos & Schombert 1995). The E+A galaxies present a peculiar spectrum in the optical: strong Balmer absorption lines, representative of a large population of A and B stars, but a *lack* of emission lines typical of blue, star-forming galaxies, such as [O II] λ3727, [O III] λ5007, and Hα. Because of the further detection of metallic absorption lines, such as Mg b λ5175, Ca H and K $\lambda\lambda$3934, 3968, and Fe λ5270, indicative of an old population dominated by G, K, and M spectral types, they were called E+A (Dressler & Gunn 1983). In addition, their spectra in the *optical* cannot be reproduced simply by modeling a young stellar component without nebular emission lines: it is necessary to add an old population of stars, like the one present in quiescent elliptical galaxies (Liu & Green 1996).

During the last 3 years, research on the E+A galaxies has seen a revival after the discovery of more such galaxies, not only in nearby clusters, such as Coma and others (see, e.g., Caldwell & Rose 1997 and references therein), but also in the field, in particular, those discovered during the Las Campanas Redshift Survey (LCRS; Shectman et al. 1996) by Zabludoff et al. (1996). An interesting feature is the apparent existence of two classes of E+A galaxies (Couch & Sharples 1987). One is formed by "blue" poststarburst galaxies and the other by redder, Hδ-strong (HDS) galaxies (Fabricant, McClintock, & Bautz 1991). These subclasses of E+A galaxies have colors and absorption-line features related to their morphology: HDS E+A galaxies have in general a noticeable bulge and/or spheroidal component when compared with the blue class. In addition, the HDS class can be divided into two subclasses: bulge and disk HDS galaxies (as observed in A665 and in Coma Franx 1993).

An almost unexplored domain of these E+A galaxies is their near-IR properties. In fact, no catalog or systematic observations exist on this subject. Is the bright, red population, dominated mainly by giants and stars of the asymptotic giant branch (AGB) of the E+A galaxies different from the red population of other elliptical galaxies, in particular the perturbed ellipticals? Is there any conspicuous signature in the near-IR colors of the E+A galaxies, as in the optical wavelengths? Do the cluster E+A galaxies have bluer colors than those in the field at these wavelengths? Are the near-IR colors of the E+A galaxies similar to the colors of normal galaxies, as predicted by spectrophotometric models?

In this paper, we investigate these questions with new data taken at Las Campanas Observatory in Chile. The sample includes E+A galaxies from the field (most of them from the LCRS) and from nearby clusters, as well as clusters at $z \sim 0.3$.

The paper is organized as follows: In § 2, we present the galaxies selected for this work. In § 3, we explain the observations, and in § 4 the data reduction procedures. In § 5, we present the results of the photometry, the apparent magnitudes, colors, and K-corrections. Both *observed* and *rest-frame* colors are compared with colors obtained from spectrophotometric models of galaxy evolution in § 6. In § 7, we discuss the limitations of our results and the implications for some properties of the E+A galaxies from our near-IR colors. Conclusions are presented in § 8.

2. THE SAMPLES

All the galaxies selected for this study have been spectroscopically classified as E+A galaxies from the analysis of

[1] Andes-Carnegie Fellow.

TABLE 1

THE SAMPLE

ID[a]	Sample[b] ID	Name[c]	R.A. (J2000.0)	Decl. (J2000.0)	z	Cluster/Field	T Type[d]	Reference[e]
E+A galaxies:								
1	1	g515	15 24 26	+08 09 06	0.0870	Abell 665	0	1
2	1	dc204852_26	20 49 52	−53 02 58	0.0397	ACO 3716	−2	2
3	1	dc184263_39m	18 42 49	−63 12 28	0.0144	DC 1842−63	−3	2
4	1	dc204852_100	20 51 49	−52 44 45	0.0493	ACO 3716	−2	2
5	1	dc204852_148	20 49 13	−52 33 51	0.0429	ACO 3716	−2	2
6	1	dc204852_39	20 50 01	−52 59 56	0.0489	ACO 3716	−2	2
7	1	dc204852_45	20 52 10	−52 56 09	0.0484	ACO 3716	−2	2
8	1	dc204852_104	20 51 07	−52 43 34	0.0493	ACO 3716	0	2
9	1	dc204852_149	20 48 30	−52 33 07	0.0569	ACO 3716	0	2
10.....	1	dc204852_192	20 51 56	−52 03 45	0.0473	ACO 3716	−5	2
11.....	1	dc204852_77	20 52 54	−52 47 28	0.0452	ACO 3716	−2	2
12.....	1	dc204852_174	20 51 46	−52 16 09	0.0448	ACO 3716	−5	2
13.....	1	dc204852_184	20 54 00	−52 08 15	0.0469	ACO 3716	−2	2
14.....	1	dc204852_216	20 49 24	−51 56 56	0.0490	ACO 3716	−2	2
15.....	1	dc204852_231	20 51 40	−51 45 22	0.0459	ACO 3716	−2	2
16.....	1	dc032952_135a	03 29 31	−52 27 18	0.0519	ACO 3128	−2	2
17.....	1	dc032952_156a	03 31 15	−52 22 28	0.0604	ACO 3128	−2	2
18.....	1	dc010746_30b	01 10 51	−45 51 52	0.0267	ACO 2877	−5	2
19.....	1	dc032952_82a	03 31 09	−52 36 49	0.0576	ACO 3128	−5	2
20.....	1	dc032952_158b	03 29 35	−52 39 58	0.0500	ACO 3128	0	2
21.....	1	dc010746_22m	01 08 23	−46 09 09	0.0200	ACO 2877	0	2
22.....	1	dc010746_45m	01 09 07	−45 44 29	0.0300	ACO 2877	0	2
23.....	2	ac103_132	20 57 18	−64 38 48	0.3047	AC 103	0	3
24.....	2	ac114_22	22 58 50	−34 48 13	0.3354	AC 114	0	3
25.....	2	ac114_89	22 58 49	−34 46 57	0.3169	AC 114	0	3
26.....	2	ac103_03	20 56 55	−64 40 11	0.3118	AC 103	0	3
27.....	2	ac103_106	20 56 47	−64 40 56	0.3091	AC 103	0	3
28.....	2	ac103_280	20 57 26	−64 42 11	0.3111	AC 103	0	3
29.....	2	ac103_145	20 57 07	−64 38 29	0.3105	AC 103	−2	3
30.....	3	lcrs01	11 01 19	−12 10 18	0.0746	Field	1	4
31.....	3	lcrs17	10 13 52	−02 55 47	0.0609	Field	0	4
32.....	3	lcrs21	11 15 24	−06 45 13	0.0994	Field	0	4
33.....	3	lcrs13	11 19 52	−12 52 39	0.0957	Field	1	4
34.....	3	lcrs14	13 57 01	−12 26 47	0.0704	Field	0	4
35.....	3	lcrs12	12 05 59	−02 54 32	0.0971	Field	1	4
36.....	3	lcrs03	12 09 05	−12 22 37	0.0810	Field	1	4
37.....	3	lcrs16	12 19 55	−06 14 01	0.0764	Field	1	4
38.....	3	lcrs15	14 40 44	−06 39 54	0.1137	Field	0	4
39.....	3	lcrs06	11 53 55	−03 10 36	0.0884	Field	0	4
40.....	3	lcrs08	14 32 03	−12 57 31	0.1121	Field	−2	4
41.....	3	lcrs07	22 41 09	−38 34 35	0.1141	Field	0	4
42.....	3	lcrs20	00 38 44	−38 57 12	0.0632	Cluster	−2	4
43.....	3	lcrs18	00 22 46	−41 33 37	0.0598	Field	0	4
44.....	3	lcrs05	01 58 01	−44 37 14	0.1172	Field	−2	4
45.....	3	lcrs19	02 07 49	−45 20 50	0.0640	Field	0	4
46.....	3	lcrs11	01 14 49	−41 22 30	0.1216	Cluster	0	4
47.....	3	lcrs02	02 17 39	−44 32 47	0.0987	Field	2	4
48.....	3	lcrs09	01 17 38	−41 24 23	0.0651	Field	0	4
49.....	3	lcrs10	02 11 43	−44 07 39	0.1049	Field	0	4
50.....	3	lcrs04	04 00 00	−44 35 16	0.1012	Cluster	1	4
Control galaxies:								
51.....	4	pgc35435	11 30 05	−11 32 47	0.0178	Field	−3	5
52.....	4	dc204852_116	20 51 19	−52 40 41	0.0441	ACO 3716	−5	2
53.....	4	dc204852_66	20 51 45	−52 51 19	0.0410	ACO 3716	−5	2
54.....	4	pgc60102	17 20 28	−00 58 46	0.0304	Field	−2	6
55.....	4	eso290-IG_050	23 06 46	−44 15 06	0.0290	Field	−2	7
56.....	4	pgc62615	18 57 41	−52 31 46	0.0280	Field	2	8
57.....	4	pgc57612	16 15 04	−60 54 26	0.0183	Field	−5	9
58.....	4	ngc6653	18 44 39	−73 15 47	0.0172	Field	−5	9
59.....	4	dc204852_115	20 51 21	−52 39 17	0.0440	ACO 3716	−5	2
60.....	4	dc204852_126	20 51 44	−52 37 57	0.0489	ACO 3716	−2	2

TABLE 1—*Continued*

ID[a]	Sample[b] ID	Name[c]	R.A. (J2000.0)	Decl. (J2000.0)	z	Cluster/Field	T Type[d]	Reference[e]
61.....	4	dc204852_38	20 50 05	−53 00 28	0.0454	ACO 3716	−2	2
62.....	4	ngc6328	17 23 41	−65 00 37	0.0142	Field	2	6
63.....	4	pgc62765	19 05 59	−42 21 59	0.0193	Field	−2	6

NOTE.—Units of right ascension are hours, minutes, and seconds, and units of declination are degrees, arcminutes, and arcseconds.

[a] Order number of the galaxy.

[b] Sample 1, nearby cluster E+A galaxies; sample 2, distant cluster E+A galaxies; sample 3, LCRS E+A galaxies; sample 4, control galaxies.

[c] Galaxy identification used in this paper.

[d] Morphological type in T-type units, from the de Vaucouleurs classification system (de Vaucoulers, de Vaucouleurs, & Corwin 1976).

[e] For quantities other than magnitudes.

REFERENCES.—(1) Franx 1993; (2) Caldwell & Rose 1997; (3) Couch & Sharples 1987; (4) Zabludoff et al. 1996; (5) Fairall et al. 1992; (6) de Vaucouleurs et al. 1991; (7) Loveday 1996; (8) Spellman, Madore, & Helou 1989; (9) Prugniel & Hérédeau 1998.

their Balmer absorption lines (particularly the equivalent widths of Hδ and Hβ) and the lack of nebular emission lines, representative of an ongoing stellar formation process. We have selected most of the southern E+A galaxies existent in the literature at present. The sample of galaxies is divided into four samples. The first sample corresponds to 21 field E+A galaxies from the LCRS selected from a catalog of $\sim$19,000 galaxies with redshift between $z \sim 0.07$ and $z \sim 0.18$ (Zabludoff et al. 1996). The second sample contains 22 E+A galaxies from the nearby clusters DC 2048−52, 1842−63, 0329−52, and 0107−46 (Caldwell & Rose 1997) at $z \sim 0.05$. Seven E+A galaxies from rich clusters at $z \sim 0.31$ (AC 103 and AC 114) constitute the third sample (Couch & Sharples 1987). Some "control" galaxies were also observed (the fourth sample, containing 13 galaxies). These galaxies have well-known properties and provide a reference sample to compare the observables of the E+A sample. The control sample includes mostly elliptical and lenticular galaxies (from clusters and the field), as well as a few galaxies between $z \sim 0.01$ and $z \sim 0.04$. Table 1 summarizes the sample of 63 galaxies that have been observed.

3. OBSERVATIONS

All of the observations presented here were carried out at Las Campanas Observatory, Chile, during photometric conditions. Most of the images were obtained with the 40 inch (1 m) Swope Telescope using a NICMOS3 HgCdTe array (256 × 256 pixels, 0.″599 pixel^{-1}, 2.′5 × 2.′5 field of view) in 1998 March, July, August, and November. We also employed the 100 inch (2.5 m) du Pont Telescope in 1998 September with a NICMOS3 detector, yielding a scale of 0.″42 pixel^{-1} (1.′8 × 1.′8 field of view). We use the J, H, and K-short (K_s) filters, centered at 1.24, 1.65, and 2.16 μm, respectively, and bandwidths of 0.22, 0.30, and 0.33 μm (for a detailed discussion of the photometric system, see Persson et al. 1998).

Between five and eight standard stars from Persson et al. (1998) were observed each night. The observation procedure for all the objects (standards included) was as follows: Each object was observed at several positions on the array, for some time in each position (I call this an *observing sequence* for a given object in a given filter). The time depended on the magnitude of the object, the sky brightness, and the linearity regime of the array. The NICMOS3 becomes noticeably nonlinear when the total counts (sky and object) exceed 17,000 ADU. We exposed in each position for 60 to 120 s in J, 30 to 60 s in H, and 30 to 50 s in K_s. Total exposure times for a given observing sequence and filter varied between 10 and 45 minutes. For the standard stars (with magnitudes K_s between $\approx$10 and $\approx$12), the exposure time ranged from 5 to 20 s in each position for each telescope. Typically, the number of nonredundant positions at which each object was observed varied between four and 10, depending on the size and/or magnitude of the object. A prereduction was made at the beginning of each observing sequence to estimate the total exposure time required to reach a minimum central signal-to-noise ratio of $\approx$12–15. This prereduction included the construction of a sky image averaging all of the stacked images for a given object (with a σ-clipping rejection threshold), the subtraction of the sky image from each individual image, and the combination after registration of the individual sky-subtracted images.

4. DATA REDUCTION

The images have to be corrected for all of the instrumental effects, namely, nonlinear deviations, dark current contribution (dark subtraction), and pixel-to-pixel response differences (flat-field division). To determine the linearity corrections, we take several dome flats with different exposure times. Then we plot the ratio of the average counts to the integration time of each frame as a function of the average counts. After normalizing, we transform the count value $I_{\rm in}$ of each pixel into $I_{\rm out} = I_{\rm in}(1 + CI_{\rm in})$, and we solve for the *constant* C, which proved to vary between 1.0×10^{-6} and 5.0×10^{-6}. At 14,000 counts, for example, which corresponds to $\sim$75% of the whole range of the signal, the departure from linearity is only 2%.

At the beginning of the night, we took series of 20 dark frames, the number of series depending on the number of different exposure times we used through the night. The flat-field images were constructed from (1) dome flats and twilight sky flats and (2) the raw science images of the night, which allowed us to construct "superflats" from the combination of the individual frames. The useful images for these superflats were those in which the objects were faint or in which a small number of objects were observed. Because galaxy fields were in general uncrowded, it was always possible to construct superflats. Typically, each superflat was constructed from no less than 30 science images for each filter. The results show that the superflats allow corrections for fringes appearing in the stacked and combined images. The fringes are present in the three filters (J, H, and K_s) but are particularly prominent in the H images. Except for the

presence of fringes, the dome flats and sky flats are quite similar to the superflats (at the 0.6% level). However, given the better photon statistics of the superflats and the fact that the fringes are better represented by the superflats, we chose the superflats to remove the pixel-to-pixel variations. From the object frames, the dark and flat-fielding corrections were made on the images using the SQIID[2] reduction package, implemented under IRAF.[3] At this stage, a mask with the bad pixels was created (using the dark images) to correct those pixels by interpolation with their neighboring pixels in all the images.

Once the linearity corrections, as well as the dark correction and flat-fielding procedures in all the raw images, were made, the procedure to obtain stacked and combined sky-subtracted images began. This part was performed using DIMSUM,[4] also implemented under IRAF. The general procedure for a given observing sequence follows:

1. A scaling factor for each image was computed using a 5 σ iterated rejection method about the mean. The scaling factor is the median of the unrejected pixels and is stored as a descriptor in the image header. This provides a first estimate for the sky level.

2. For each image in the observing sequence, a specified number of neighboring images of the sequence were selected. To construct a sky image, we selected only the neighboring images taken within ± 5 minutes from the given image. This provides a sample of sky images within a short time, when the variations of the sky level are not larger than 1% to 3% of the mean, to reduce the rms variation in the thermal emission background, as well as the OH sky lines, characteristic of the near-IR (see Fig. 1). Furthermore, the higher background in K_s produces higher shot noise even if this background did not vary with time. This is a key step. At each pixel, a specified number of low and high values in the scaled images were rejected and the average of the remainder values was taken as the sky value for that pixel. The resulting sky image was subtracted from the object image to create a sky-subtracted object image.

3. Cosmic rays were found using a threshold algorithm applied to the ratio of the image to a median-filtered image. The detected cosmic rays were replaced by the local median. A cosmic-ray mask was created to record the location of the cosmic rays.

4. For a given observing sequence, a shift list is created to define the offsets between the images. To create this list, it is first necessary to have at least one object in common among all the images of the observing sequence (usually a star). Next we selected a set of additional objects to improve the determination of the relative shifts. These objects were used in constructing the shift list using a centroid-based algorithm.

5. A registration stage was done by shifting and combining the images of the sequence. A matching exposure map, which allows us to obtain a final mosaic properly weighted by the effective exposure time of each section of the mosaic, was also created.

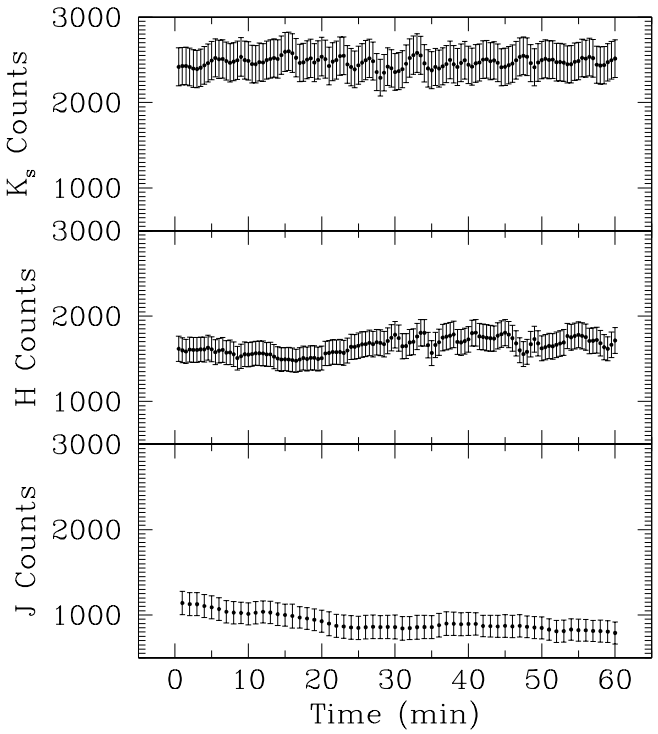

FIG. 1.—Typical sky variations in the near-IR passbands J, H, and K_s during 1 hr. Each point represents the mean sky level for an individual image during an observing sequence. The error bars are given by the standard deviation in the image counts. Note the larger error bars for the K_s band, where the thermal variations are in fact larger (also where the shot noise is higher, compared with that of other filters). This behavior limits the accuracy of the sky subtraction procedure applied to the near-IR images (see text).

6. To provide combined images free of "holes" arising from the sky subtraction, two different masks are created for each registered image of the observing sequence. The detailed procedure is explained in the DIMSUM package.

7. The sky subtraction is repeated as in the first pass, before the masking procedure, except that the pixels in the individual masks derived from step 6 are ignored.

8. Finally, all the sky-subtracted images of an observing sequence are shifted and combined and the different parts of the mosaic are scaled to an exposure time of 1 s.

5. PHOTOMETRY

5.1. *Photometric Calibrations*

The photometric calibrations were performed using the faint standard stars from the list of Persson et al. (1998). This list includes standard magnitudes in J, H, K, and K_s for equatorial and southern photometric standard stars. Five to eight standards were observed every night at air masses similar to those of the galaxies (no larger than 1.2). This minimizes the dimming and reddening due to the air-mass contribution, especially in colors involving the J filter.

Instrumental magnitudes were computed using the code SExtractor (Bertin & Arnouts 1996), which computes isophotal, isophotal-corrected, and total magnitudes for all the objects detected above a given threshold. We have also computed instrumental aperture magnitudes using

[2] Simultaneous Quad-Color Infrared Imaging Device software package, developed by M. Merrill & J. Mac Kenty.

[3] IRAF is distributed by the National Optical Astronomy Observatories, operated by the Association of Universities for Research in Astronomy, Inc., under cooperative agreement with the National Science Foundation.

[4] DIMSUM is the Deep Infrared Mosaicing Software package, developed by P. Eisenhardt, M. Dickinson, A. Stanford, & J. Ward, and is available from ftp://iraf.noao.edu/iraf/contrib/dimsumV2/dimsum.tar.Z.

DAOPHOT and verified that DAOPHOT aperture magnitudes for the standards do not differ by more than 0.5% from the total magnitudes yielded by SExtractor. The aperture used for the standards in DAOPHOT is the maximum aperture after analyzing the shape of the growth curve for the instrumental magnitudes and typically takes radius values $\sim 6''.0$. We conclude that the instrumental magnitudes given by SExtractor are reliable, and we adopt them hereafter.

The adopted photometric transformations between the instrumental and the calibrated magnitudes are

$$J = A_1 + j - 0.10X\ , \quad (1)$$

$$H = A_2 + h - 0.04X\ , \quad (2)$$

$$K_s = A_3 + k_s - 0.08X\ , \quad (3)$$

where the coefficients A_N ($N = 1, 2, 3$) are the zero points, X is the air mass, and the extinction coefficients are from Persson et al. (1998). Note that we do not try to solve for air-mass corrections night by night, as this can lead to spurious values for coefficients if the extinction is variable and nongray. The latter is relevant at the filter passband edges, where water vapor influences the effective width of the passband (Persson et al. 1998).

The zero points A_1, A_2, and A_3 were determined on a nightly basis and proved to vary between 1% and 7%. We do not include color terms in these transformations (eqs. [1]–[3]) since they are smaller than 0.04 mag, a value close to the observational magnitude errors. We emphasize that all of the standards and the galaxies reported in this paper were observed during completely photometric nights. The photometric transformations have typical rms residuals of $\sim$0.02–0.05 mag on each telescope (see Fig. 2). This gives an internal error in the photometric calibrations of about 2% to 5%.

The main sources of error are, in fact, the short-term sky fluctuations (in particular in K_s), which are on the order of 3% to 6% in time intervals spanning the longest exposure time of individual frames during each of the observing sequences (120 s in J, 60 s in H, and 50 s in K_s). Some galaxies were observed twice, even using the two telescopes, and therefore there is a good estimate of the global photometric errors, which prove to be about 7% for photometric nights. The observation of the same object during two photometric nights but with a different telescope or other

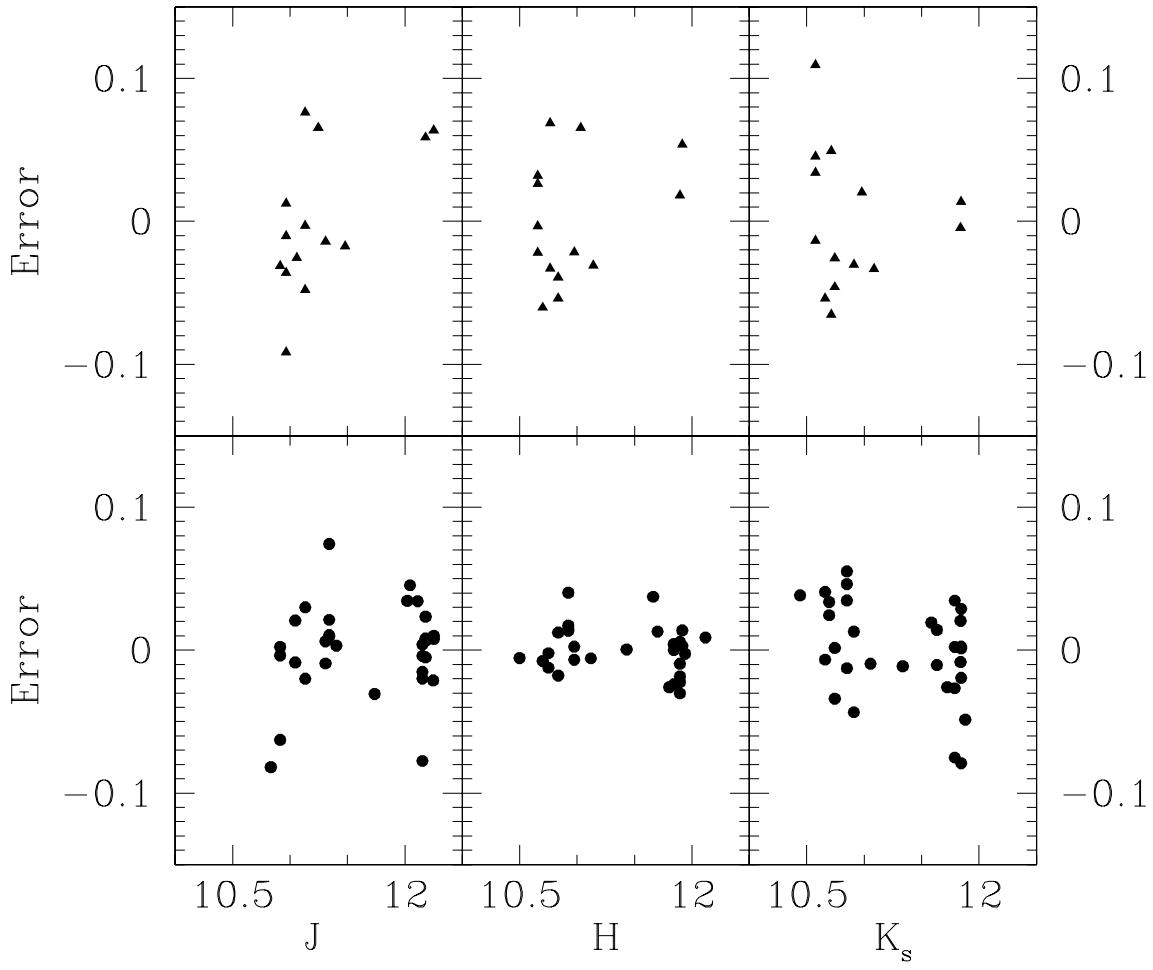

FIG. 2.—Average errors in the photometric calibrations for the standards observed with the 100 inch du Pont Telescope (*triangles*) and for the standards observed with the 40 inch Swope Telescope (*circles*). Every point corresponds to an average error of several (typically not less than three) measurements for the same standard, observed on different nights.

instrument is the best way to estimate the photometric quality of the data (see § 5.2) and the real dispersion of magnitudes.

5.2. *Galaxy Photometry*

Instrumental apparent magnitudes for all the galaxies were obtained on the registered and combined images using the code SExtractor (Bertin & Arnouts 1996). Given the differences in size, shape, and luminosity of the galaxies, the total magnitude is a better estimator than the aperture or isophotal magnitude. SExtractor computes aperture magnitudes, isophotal magnitudes, and "total" magnitudes for all the objects detected above a given threshold. The total apparent instrumental magnitude for a given object is computed by using (1) an *adaptive* aperture magnitude or (2) a *corrected* isophotal magnitude. To give the best estimate of the total magnitude, the adaptive aperture method is used, except that when a neighbor is suspected of biasing the magnitude by more than 0.1, the corrected isophotal magnitude is taken as the total magnitude. This yields the so-called MAG_BEST magnitude, in the SExtractor output catalog.

To check the calibrated magnitudes for our galaxies and to have an idea of the accuracy of our total magnitudes, we observed some of the galaxies on two different nights with the 40 inch and the 100 inch telescopes. For the eight galaxies that were observed twice (two for each sample), we found rms differences $\Delta J = 0.037$, $\Delta H = 0.042$, and $\Delta K_s = 0.061$. These differences, although large when taken at face value, represent the most realistic errors in the total magnitudes, since they were obtained with different instrumental setups during different observing runs.

5.3. *Apparent Magnitudes and K-Corrections*

Once the instrumental magnitudes are calculated using SExtractor, they are transformed to the standard system using the package PHOTCAL in IRAF. Table 2 shows the apparent calibrated total magnitudes for all of the galaxies of the four subsamples. The K_s magnitude for galaxy 25, AC 114_89, was not computed since it was observed under possibly nonphotometric conditions, and it was marked "NC" (not calibrated) in Table 2. No internal reddening correction was applied to these magnitudes, nor was a Galactic foreground extinction correction applied: both corrections are smaller than the photometric error and, in particular, are smaller than the uncertainty given by the K-correction, as we show in § 5.3. The reddening by dust is $\Delta(J-H) \lesssim 0.03$ and $\Delta(H-K_s) \lesssim 0.02$ if we consider a simple screen model based on the reddening law of Cardelli, Clayton, & Mathis (1989). If we consider a more complicated extinction model, following the star-dust mixture recipe by Wise & Silva (1996), the amount of reddening is similar. The correction due to Galactic extinction is also small for the three passbands ($\lesssim 0.03$), which proves to be well within the photometric uncertainties (for the Galactic reddening corrections in the near-IR photometric bands, see Schlegel, Finkbeiner, & Davis 1998). We emphasize, however, that Galactic and internal reddening corrections are systematic effects, while the photometric uncertainty is random. Given their small values, no attempt is made to correct for the extinctions. If we include foreground and internal extinction, the $J-H$ color reddens probably no more than 0.03–0.05 (but see discussion at the end of § 6).

Since the K-terms can significantly modify the intrinsic colors of the galaxies, they are critical in correcting the observed colors and magnitudes to the galaxy rest frame. If m_1 and m_2 are the apparent magnitudes in passbands 1 and 2, respectively, for a galaxy at redshift z of known spectral type T, then the rest-frame color for this galaxy is

$$M_1 - M_2 = m_1 - m_2 - [K_1(z, T) - K_2(z, T)] , \quad (4)$$

where M_1 and M_2 are the corresponding absolute magnitudes and $K_1(z, T)$ and $K_2(z, T)$ are the K-corrections for passbands 1 and 2, respectively, for the galaxy of spectral type T at redshift z. K-corrections are not included in the magnitudes and colors presented in Table 2, since they can have a wide range of values depending on the spectral energy distribution (SED) employed in their computation. When the SED is not available for a given object, it is common practice (although risky) to adopt K-terms from the correlation between spectral type and morphological classification, provided the latter is available.

In our case, we have only approximate morphological types for the E+A galaxies from the literature, and we do not have spectral information for the galaxies in the near-infrared part of the spectra. Even though most of our E+A galaxies are early types, we can ask the following: How will the near-IR K-corrections depend on the spectrophotometric model of galaxy evolution used to compute them? To study the model dependence in J, H, and K, for example, take two SED models that provide (or allow us to compute) K-terms in the near-IR. The first K-terms were taken directly from Poggianti (1997), who computed K-corrections from the near-UV to the infrared. Poggianti (1997) provides K-corrections in several bands in the Johnson–Bessel & Brett photometric system, up to $z = 3$ as a function of morphological type. The values are computed according to an evolutionary synthesis model that reproduces the integrated galaxy spectrum in the range 1000–25000 Å and uses the code GISSEL93 (Bruzual & Charlot 1993). The models are instantaneous bursts with solar metallicity and Scalo initial mass function (IMF; Scalo 1986). The age after the burst gives the SED, which is compared through colors with that of galaxies of known morphological type. Note that the comparison is done in the optical part of the spectrum, mostly between 3000 and 8000 Å. The second set of K-corrections were derived using the model PEGASE[5] (Fioc & Rocca-Volmerange 1997) to generate synthetic spectra between 7000 and 30000 Å and convolving these SEDs with the filter response functions (see Persson et al. 1998), using the definition of the K-correction (Oke & Sandage 1968).

Figure 3 shows the K-corrections in J, H, and K, calculated by Poggianti (1997) for three different morphological types, namely, E (*solid line*), Sa (*dotted line*), and Sc (*dashed line*). Note that the K-corrections in the near-IR are not necessarily small. Nevertheless, in most of the photometric bands they do not depend strongly on the spectral type or the morphological type. K-corrections are large (and negative) for the K band, $z \gtrsim 0.5$, for all galaxy types (this makes galaxies appear brighter than they really are). The average redshift in our sample is ≈ 0.08, and K-corrections in all the bands are less than 0.1 mag for most cases. The

[5] Projet d'etude des galaxies par synthèse evolutive.

TABLE 2

APPARENT MAGNITUDES AND COLORS

No.	Galaxy	J[a]	H[a]	K_s[a]	$J-H$	$H-K_s$	$J-K_s$	z	B[b]	R[c]	Sample[d]	T type[e]
1.....	g515	13.86 ± 0.02	13.11 ± 0.05	12.75 ± 0.05	0.75 ± 0.05	0.36 ± 0.07	1.11 ± 0.05	0.0870	...	...	1	0
2.....	dc204852_26	13.82 ± 0.03	13.16 ± 0.04	12.99 ± 0.03	0.66 ± 0.05	0.17 ± 0.05	0.83 ± 0.04	0.0397	16.99	15.38	1	−2
3.....	dc184263_39m	11.01 ± 0.02	10.27 ± 0.06	10.05 ± 0.03	0.74 ± 0.06	0.22 ± 0.07	0.96 ± 0.04	0.0144	...	...	1	−3
4.....	dc204852_100	14.62 ± 0.04	13.95 ± 0.06	13.64 ± 0.03	0.67 ± 0.07	0.31 ± 0.07	0.98 ± 0.05	0.0493	17.61	16.19	1	−2
5.....	dc204852_148	14.44 ± 0.04	13.74 ± 0.06	13.44 ± 0.04	0.70 ± 0.07	0.30 ± 0.07	1.00 ± 0.06	0.0429	17.57	16.01	1	−2
6.....	dc204852_39	14.50 ± 0.03	13.81 ± 0.05	13.48 ± 0.03	0.69 ± 0.06	0.33 ± 0.06	1.02 ± 0.04	0.0489	17.77	16.16	1	−2
7.....	dc204852_45	15.04 ± 0.04	14.39 ± 0.05	14.03 ± 0.03	0.65 ± 0.06	0.36 ± 0.06	1.01 ± 0.05	0.0484	...	...	1	−2
8.....	dc204852_104	14.99 ± 0.05	14.25 ± 0.05	13.95 ± 0.04	0.74 ± 0.07	0.30 ± 0.06	1.04 ± 0.06	0.0493	...	...	1	0
9.....	dc204852_149	13.91 ± 0.03	13.24 ± 0.05	12.91 ± 0.04	0.67 ± 0.06	0.33 ± 0.06	1.00 ± 0.05	0.0569	...	...	1	0
10.....	dc204852_192	13.83 ± 0.05	13.13 ± 0.04	12.80 ± 0.05	0.70 ± 0.06	0.33 ± 0.06	1.03 ± 0.07	0.0473	16.98	15.40	1	−5
11.....	dc204852_77	14.88 ± 0.03	14.16 ± 0.04	13.90 ± 0.04	0.72 ± 0.05	0.26 ± 0.06	0.98 ± 0.05	0.0452	...	...	1	−2
12.....	dc204852_174	14.84 ± 0.03	14.15 ± 0.05	13.88 ± 0.03	0.69 ± 0.06	0.27 ± 0.06	0.96 ± 0.04	0.0448	18.09	16.43	1	−5
13.....	dc204852_184	14.29 ± 0.02	13.60 ± 0.04	13.25 ± 0.04	0.69 ± 0.04	0.35 ± 0.06	1.04 ± 0.04	0.0469	17.36	15.78	1	−2
14.....	dc204852_216	13.87 ± 0.04	13.18 ± 0.03	12.88 ± 0.02	0.69 ± 0.05	0.30 ± 0.04	0.99 ± 0.04	0.0490	...	...	1	−2
15.....	dc204852_231	13.58 ± 0.03	12.88 ± 0.03	12.58 ± 0.03	0.70 ± 0.04	0.30 ± 0.04	1.00 ± 0.04	0.0459	16.72	15.18	1	−2
16.....	dc032952_135a	14.34 ± 0.02	13.52 ± 0.04	13.09 ± 0.04	0.82 ± 0.04	0.43 ± 0.06	1.25 ± 0.04	0.0519	18.09	16.21	1	−2
17.....	dc032952_156a	13.22 ± 0.04	12.48 ± 0.03	12.15 ± 0.03	0.74 ± 0.05	0.33 ± 0.04	1.07 ± 0.05	0.0604	16.61	14.93	1	−2
18.....	dc010746_30b	14.99 ± 0.07	14.42 ± 0.04	14.21 ± 0.03	0.57 ± 0.08	0.21 ± 0.05	0.78 ± 0.08	0.0267	17.90	16.41	1	−5
19.....	dc032952_82a	14.96 ± 0.03	14.35 ± 0.03	14.18 ± 0.03	0.61 ± 0.04	0.17 ± 0.04	0.78 ± 0.04	0.0576	17.81	16.42	1	−5
20.....	dc032952_158b	14.13 ± 0.03	13.41 ± 0.02	13.02 ± 0.04	0.72 ± 0.04	0.39 ± 0.04	1.11 ± 0.05	0.0500	17.26	15.76	1	0
21.....	dc010746_22m	14.49 ± 0.04	13.87 ± 0.04	13.60 ± 0.02	0.62 ± 0.06	0.27 ± 0.04	0.89 ± 0.04	0.0200	...	...	1	0
22.....	dc010746_45m	14.98 ± 0.03	14.32 ± 0.04	14.16 ± 0.03	0.66 ± 0.05	0.16 ± 0.05	0.82 ± 0.04	0.0300	17.37	16.24	1	0
23.....	ac103_132	18.45 ± 0.08	18.24 ± 0.07	17.23 ± 0.06	0.21 ± 0.10	1.01 ± 0.09	1.22 ± 0.10	0.3047	...	19.34	2	6
24.....	ac114_22	18.26 ± 0.08	17.57 ± 0.06	16.76 ± 0.07	0.69 ± 0.10	0.81 ± 0.09	1.50 ± 0.11	0.3354	...	19.85	2	0
25.....	ac114_89	17.79 ± 0.09	17.24 ± 0.07	NC	0.55 ± 0.11	...	...	0.3169	...	19.78	2	0
26.....	ac103_03	16.33 ± 0.08	15.44 ± 0.08	15.09 ± 0.05	0.89 ± 0.11	0.35 ± 0.09	1.24 ± 0.09	0.3118	19.95	18.12	2	0
27.....	ac103_106	17.15 ± 0.09	16.34 ± 0.07	15.76 ± 0.06	0.81 ± 0.11	0.58 ± 0.09	1.39 ± 0.11	0.3091	...	...	2	0
28.....	ac103_280	17.21 ± 0.06	16.23 ± 0.07	15.76 ± 0.07	0.98 ± 0.09	0.47 ± 0.10	1.45 ± 0.09	0.3111	21.00	18.93	2	0
29.....	ac103_145	17.20 ± 0.08	16.31 ± 0.08	15.90 ± 0.07	0.89 ± 0.11	0.41 ± 0.11	1.30 ± 0.10	0.3105	...	19.66	2	3
30.....	lcrs01	16.18 ± 0.04	15.57 ± 0.05	15.10 ± 0.04	0.61 ± 0.06	0.47 ± 0.06	1.08 ± 0.06	0.0746	...	17.05	3	1
31.....	lcrs17	15.83 ± 0.03	15.19 ± 0.03	14.75 ± 0.05	0.64 ± 0.04	0.44 ± 0.06	1.08 ± 0.06	0.0609	...	16.99	3	0
32.....	lcrs21	15.55 ± 0.03	14.94 ± 0.04	14.53 ± 0.04	0.61 ± 0.05	0.41 ± 0.06	1.02 ± 0.05	0.0994	...	16.93	3	0
33.....	lcrs13	14.49 ± 0.03	13.67 ± 0.02	13.29 ± 0.03	0.82 ± 0.04	0.38 ± 0.04	1.20 ± 0.04	0.0957	...	12.97	3	1
34.....	lcrs14	14.90 ± 0.03	14.20 ± 0.05	13.77 ± 0.03	0.70 ± 0.06	0.43 ± 0.06	1.13 ± 0.04	0.0704	...	16.05	3	0
35.....	lcrs12	15.02 ± 0.03	14.35 ± 0.04	13.82 ± 0.03	0.67 ± 0.05	0.53 ± 0.05	1.20 ± 0.04	0.0971	...	16.78	3	1
36.....	lcrs03	14.11 ± 0.04	13.47 ± 0.03	13.04 ± 0.03	0.64 ± 0.05	0.43 ± 0.04	1.07 ± 0.05	0.0810	...	15.03	3	1
37.....	lcrs16	15.35 ± 0.04	14.75 ± 0.04	14.41 ± 0.03	0.60 ± 0.06	0.34 ± 0.05	0.94 ± 0.05	0.0764	...	16.69	3	1
38.....	lcrs15	15.84 ± 0.05	15.16 ± 0.05	14.73 ± 0.04	0.68 ± 0.07	0.43 ± 0.06	1.11 ± 0.06	0.1137	...	17.19	3	0
39.....	lcrs06	15.64 ± 0.05	15.09 ± 0.04	14.72 ± 0.03	0.55 ± 0.06	0.37 ± 0.05	0.92 ± 0.06	0.0884	...	16.81	3	0
40.....	lcrs08	15.63 ± 0.04	15.01 ± 0.03	14.55 ± 0.04	0.62 ± 0.05	0.46 ± 0.05	1.08 ± 0.06	0.1121	...	17.87	3	−2
41.....	lcrs07	13.62 ± 0.05	12.89 ± 0.03	12.45 ± 0.04	0.73 ± 0.06	0.44 ± 0.05	1.17 ± 0.06	0.1141	...	15.00	3	0
42.....	lcrs20	14.48 ± 0.03	13.89 ± 0.03	13.53 ± 0.05	0.59 ± 0.04	0.36 ± 0.06	0.95 ± 0.06	0.0632	...	15.96	3	−2
43.....	lcrs18	14.70 ± 0.04	14.02 ± 0.03	13.62 ± 0.03	0.68 ± 0.05	0.40 ± 0.04	1.08 ± 0.05	0.0598	...	16.09	3	0
44.....	lcrs05	15.36 ± 0.05	14.80 ± 0.03	14.32 ± 0.05	0.56 ± 0.06	0.48 ± 0.06	1.04 ± 0.07	0.1172	...	16.73	3	−2
45.....	lcrs19	14.95 ± 0.03	14.24 ± 0.04	13.90 ± 0.03	0.71 ± 0.05	0.34 ± 0.05	1.05 ± 0.04	0.0640	...	16.42	3	0
46.....	lcrs11	15.48 ± 0.04	14.78 ± 0.04	14.38 ± 0.03	0.70 ± 0.06	0.40 ± 0.05	1.10 ± 0.05	0.1216	...	16.96	3	0
47.....	lcrs02	14.95 ± 0.03	14.28 ± 0.03	13.95 ± 0.03	0.67 ± 0.04	0.33 ± 0.04	1.00 ± 0.04	0.0987	...	16.36	3	2

TABLE 2—*Continued*

No.	Galaxy	J^a	H^a	K_s^a	$J-H$	$H-K_s$	$J-K_s$	z	B^b	R^c	Sample[d]	T type[e]
48.....	lcrs09	15.98 ± 0.05	15.30 ± 0.04	14.96 ± 0.03	0.68 ± 0.06	0.34 ± 0.05	1.02 ± 0.06	0.0651	...	17.47	3	0
49.....	lcrs10	15.29 ± 0.04	14.65 ± 0.05	14.27 ± 0.04	0.64 ± 0.06	0.38 ± 0.06	1.02 ± 0.05	0.1049	...	16.68	3	0
50.....	lcrs04	14.49 ± 0.04	13.80 ± 0.05	13.41 ± 0.03	0.69 ± 0.06	0.39 ± 0.06	1.08 ± 0.05	0.1012	...	15.68	3	1
51.....	pgc35435	11.75 ± 0.03	10.98 ± 0.04	10.66 ± 0.02	0.77 ± 0.05	0.32 ± 0.04	1.09 ± 0.04	0.0178	13.75	...	4	−3
52.....	dc204852_116	12.62 ± 0.06	11.92 ± 0.05	11.65 ± 0.02	0.70 ± 0.08	0.27 ± 0.05	0.97 ± 0.06	0.0441	15.84	14.06	4	−5
53.....	dc204852_66	14.45 ± 0.05	13.62 ± 0.04	13.36 ± 0.03	0.83 ± 0.06	0.26 ± 0.05	1.09 ± 0.06	0.0410	17.48	15.88	4	−5
54.....	pgc60102	12.96 ± 0.06	12.13 ± 0.03	11.65 ± 0.04	0.84 ± 0.07	0.47 ± 0.05	1.31 ± 0.07	0.0304	15.36	...	4	−2
55.....	eso290-IG_050	13.46 ± 0.03	12.74 ± 0.03	12.39 ± 0.03	0.72 ± 0.04	0.35 ± 0.04	1.07 ± 0.04	0.0290	15.18	14.21	4	−2
56.....	pgc62615	12.65 ± 0.04	11.92 ± 0.04	11.63 ± 0.04	0.73 ± 0.06	0.29 ± 0.06	1.02 ± 0.06	0.0280	...	...	4	2
57.....	pgc57612	10.99 ± 0.03	10.22 ± 0.03	10.10 ± 0.03	0.77 ± 0.04	0.11 ± 0.04	0.88 ± 0.04	0.0183	13.30	11.33	4	−5
58.....	ngc6653	11.53 ± 0.04	10.79 ± 0.01	10.59 ± 0.04	0.74 ± 0.04	0.20 ± 0.04	0.94 ± 0.06	0.0172	...	...	4	−5
59.....	dc204852_115	14.98 ± 0.03	14.33 ± 0.03	14.04 ± 0.03	0.65 ± 0.04	0.29 ± 0.04	0.94 ± 0.04	0.0440	18.13	16.53	4	−5
60.....	dc204852_126	15.01 ± 0.04	14.29 ± 0.04	14.01 ± 0.04	0.72 ± 0.06	0.28 ± 0.06	1.00 ± 0.06	0.0489	18.21	16.60	4	−2
61.....	dc204852_38	13.49 ± 0.05	12.90 ± 0.03	12.56 ± 0.04	0.59 ± 0.06	0.34 ± 0.05	0.93 ± 0.06	0.0454	16.73	15.12	4	−2
62.....	ngc6328	11.33 ± 0.03	10.57 ± 0.04	10.24 ± 0.04	0.77 ± 0.05	0.32 ± 0.06	1.09 ± 0.05	0.0142	13.17	11.45	4	2
63.....	pgc62765	11.42 ± 0.04	10.68 ± 0.04	10.36 ± 0.03	0.74 ± 0.06	0.32 ± 0.05	1.06 ± 0.05	0.0193	...	...	4	−2

[a] Apparent magnitude and photometric error.
[b] Apparent total magnitude in the Johnson system provided by NED.
[c] Apparent total magnitude in the Cousins system provided by NED.
[d] See Table 1.
[e] Morphological T-type provided by NED.

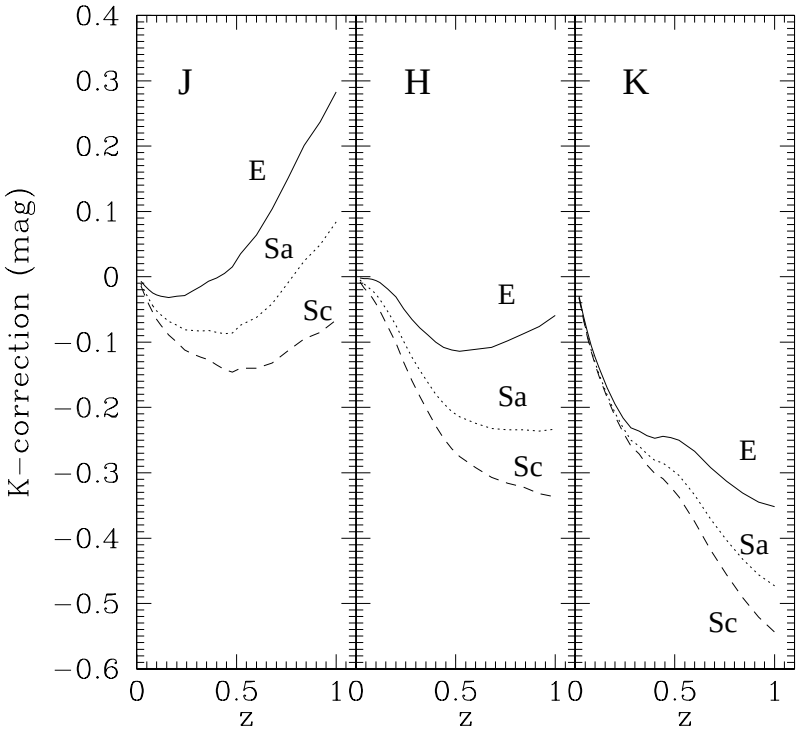

FIG. 3.—*K*-corrections from the models of Poggianti (1997) for passbands *J*, *H*, and *K* for redshifts between 0 and 1 and for Hubble types E (*solid line*), Sa (*dotted line*), and Sc (*dashed line*). Note the large negative *K*-corrections for the *K* band for $z \gtrsim 0.5$.

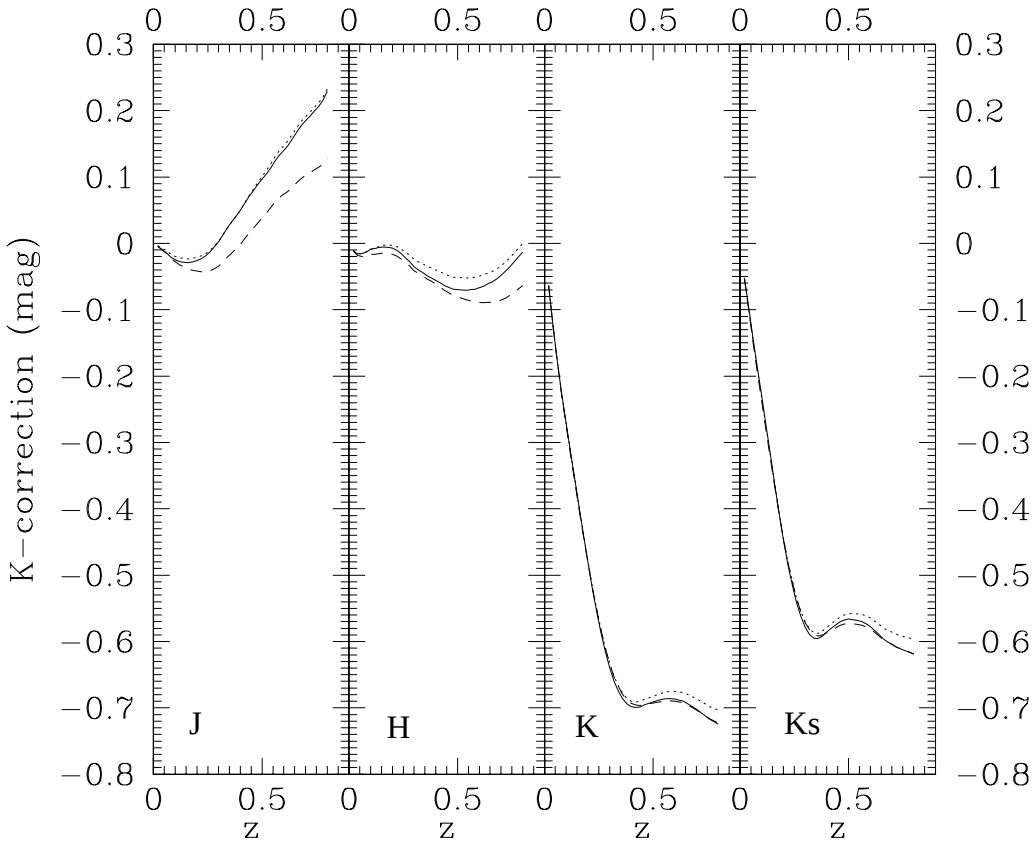

FIG. 4.—*K*-corrections derived from the PEGASE models (Fioc & Rocca-Volmerange 1997) for the *J*, *H*, *K*, and K_s bands as a function of redshift and Hubble type (lines as in Fig. 3). Compare with Fig. 3.

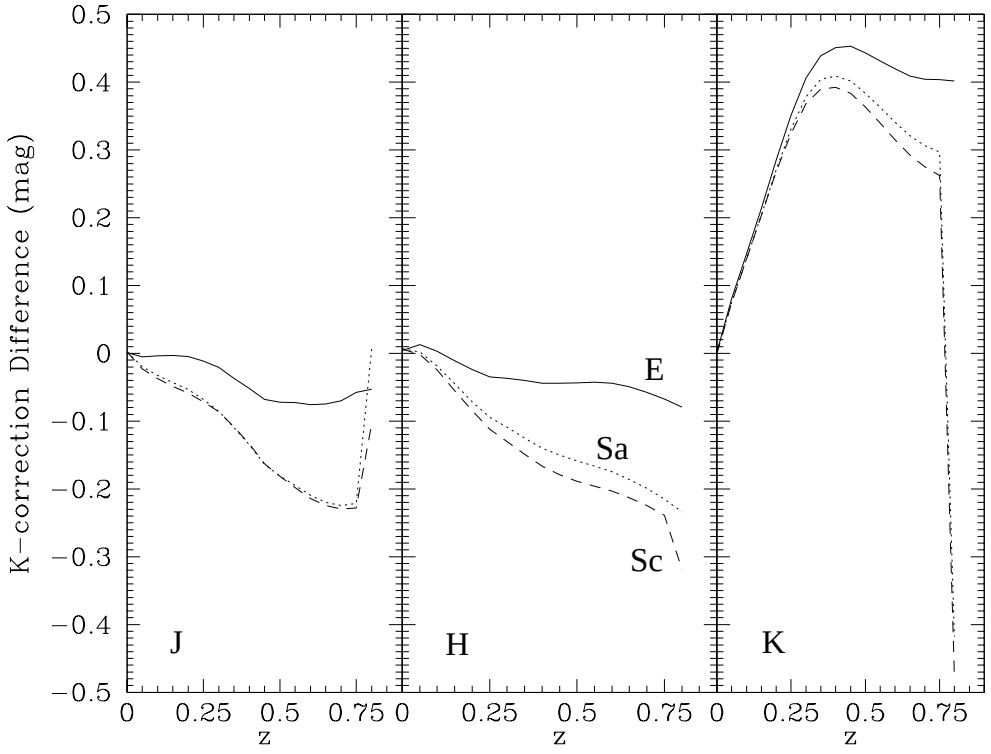

FIG. 5.—K-correction differences obtained from two spectrophotometric models of galaxy evolution, indicated in Figs. 3 and 4. Differences are computed for J, H, and K and for Hubble types E, Sa, and Sc. Note the large difference for the K-corrections in the K band.

exceptions are the E+A galaxies in AC 103 and AC 104 (at $z \sim 0.3$). For these objects, K-corrections can be larger, about -0.3 mag in K for the late-type galaxies. Figure 4 shows the K-term calculated from PEGASE. These K-corrections are calculated from SEDs with solar metallicity and instantaneous bursts. The IMF is from Scalo (1986). In PEGASE, the authors define their morphological types by directly comparing spectra generated from their models with Kennicutt (1992) optical spectra of nearby galaxies. Poggianti (1997), on the other hand, matches colors obtained from her model with observed colors of galaxies taken from Persson, Frogel, & Aaronson (1979) and Bower, Lucey, & Ellis (1992a, 1992b).

Comparing Figures 3 and 4, we conclude that although the K-corrections are quite different from one model to another, they are similar for $z \lesssim 0.1$. For $z \gtrsim 0.2$, differences are larger. K-corrections for different Hubble types are more similar if they are derived from PEGASE rather than from the models of Poggianti. Figure 5 shows the differences between these K-corrections for the two models in the three passbands for the three Hubble types. Up to $z \sim 0.5$, the difference for the E type in J and H is less than 0.05 mag. However, the difference is ~ 0.1 mag for the later types. Equation (4) implies that the differences in $J-H$ will be less than 0.05 mag. However, this is not the case for colors involving the K band ($J-K$ and $H-K$) because of the large difference in the K-corrections for all the Hubble types, as also shown in Figure 5. The difference in K for the K-corrections reaches ~ 0.4 mag at $z \sim 0.3$. This shows that K-correction uncertainty will have the largest impact on rest-frame colors. Other studies also show large differences in their K-corrections, although some of them are comparable to the values of this work, showing large negative K-corrections in K (Frogel et al. 1978; Persson et al. 1979; Bershady 1995). For example, Bershady (1995) obtains type-averaged K-corrections in K that reach -0.33 and -0.60 at $z = 0.14$ and $z = 0.30$, respectively. These values are larger than those from Poggianti (1997) but similar to those obtained from PEGASE (see Figs. 3 and 4).

6. COMPARISON WITH MODELS

As shown in the preceding section, K-corrections in the near-IR can be very different depending on the spectrophotometric models used. Therefore, we do not use rest-frame colors, i.e., we do not deredshift the data. Instead, we redshift current-epoch SEDs. Although this approach is similar to work with rest-frame colors, it is more robust, since the SEDs of the current-epoch models can be determined absolutely. To give an idea of whether synthetic SEDs compare well with spectra of galaxies at the current epoch, we consider GISSEL96 models (Charlot, Worthey, & Bressan 1996) and compare them with real, local galaxy spectra of known morphological types, given by Kennicutt (1992). As is well known, the age-metallicity degeneracy prevents us for deriving age and metallicity directly from colors, as was shown by Worthey (1994) and Ferreras, Charlot, & Silk (1999). Therefore, we consider instantaneous bursts of fixed (solar) metallicity. Subsequent evolution is determined by adopting passive stellar evolution, measured in gigayears and indicated by the label on each model spectrum in Figure 6. A simple χ^2 test is used to determine the model spectra closest to the observed (Kennicutt) sample. We use a starting sample of 20 GISSEL96 spectra and 27 spectra representative of normal galaxies of known Hubble types (Galaz & de Lapparent 1998). Figure 6 shows the better spectral match between some Kennicutt spectra and the 20 selected GISSEL96 models.

The Hubble sequence fits well with an evolutionary

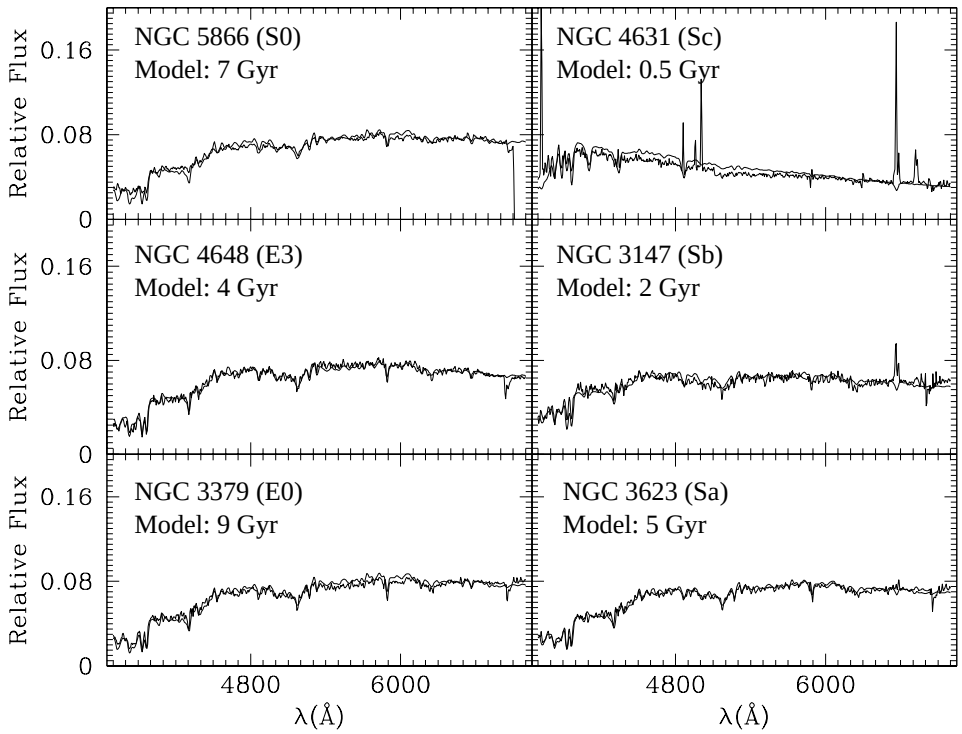

FIG. 6.—Some Kennicutt (1992) spectra of observed normal galaxies with known Hubble types (*thick lines*) and fitted synthetic spectra from GISSEL96 (Charlot, Worthey, & Bressan 1996; *thin lines*). The fitted models correspond to instantaneous bursts of solar metallicity and different ages of the passively evolving stellar populations. The closest model spectrum is obtained using a simple χ^2-fitting algorithm between the Kennicutt spectra and 20 model spectra. The good match shows that at the optical wavelengths, models agree with observations. The same kind of models are compared for the near-IR colors. See text for details.

sequence in the optical, but care has to be taken in the interpretation since more than one solution can be obtained from a synthetic set in which both age and metallicity vary (Ronen, Aragón-Salamanca, & Lahav 1999). Even though metallicity can vary from one galaxy to another, it is realistic to set metallicity close to solar. Extremely metal-poor ($Z \lesssim 0.5\ Z_\odot$) or metal-rich ($Z \gtrsim 1.5\ Z_\odot$) cases are unlikely in this set of galaxies (Liu & Green 1996). Moreover, the fact that colors are obtained from *integrated* total apparent magnitudes implies that colors are an average over the whole galaxy light and therefore are likely to be representative of solar or lower metallicity in the luminosity-weighted mean (see, e.g., Edmunds 1992).

To compare the observed colors with models, we take the 20 spectra from GISSEL96, and we "redshift" them to several redshift values (from the rest frame to $z = 0.5$). Afterward, we compute synthetic colors using the J, H, and K_s passbands (Persson et al. 1998) for the 20 synthetic spectra. Figure 7 shows the color-color diagram for the E+A sample and the control sample (*filled circles*), as well as for the model spectra (*open symbols*) for redshifts (*bottom right*). We include in Figure 7 three different evolving tracks for instantaneous bursts: after 1 Gyr (*circles*), 3 Gyr (*squares*), and 16 Gyr (*triangles*). After 10 Gyr, the near-IR colors are almost independent of age for a given redshift.

Figure 7 shows an overall agreement between near-IR colors of all samples and models, except for sample 3. The average color $\langle H-K_s\rangle = 0.41$ ($\sigma = 0.05$) of sample 1 (average redshift $\langle z\rangle = 0.09$, $\sigma = 0.02$) agrees well with any model older than 3 Gyr at $z = 0.10$. However, the average $\langle J-H\rangle = 0.66$ ($\sigma = 0.06$) appears bluer than the same models by ~ 0.1 mag. Otherwise, $\langle J-H\rangle$ is well fitted by a model with age $\lesssim 3$ Gyr at $z = 0.10$, but then $\langle H-K_s\rangle$ of sample 1 is redder by ~ 0.1 mag. These differences are twice the color dispersion for this sample. Therefore we can conclude that colors of the models and the data do not differ by more than 2 σ. In sample 2, the average colors $\langle H-K_s\rangle = 0.29$ ($\sigma = 0.07$) and $\langle J-H\rangle = 0.69$ ($\sigma = 0.05$) with average redshift $\langle z\rangle = 0.046$ ($\sigma = 0.014$) are well fitted by a model at $z = 0.05$ and 2.8 Gyr. Sample 3, having $\langle H-K_s\rangle = 0.61$ ($\sigma = 0.23$), $\langle J-H\rangle = 0.75$ ($\sigma = 0.25$), and average redshift $\langle z\rangle = 0.31$ ($\sigma = 0.01$), is not fitted by the GISSEL96 models, even though the average color $\langle H-K_s\rangle$ is closer to the $z = 0.3$ redshifted color of the models. Sample 4 (the control sample) matches the model colors well, despite the rather large scatter. This sample has average colors $\langle H-K_s\rangle = 0.29$ ($\sigma = 0.08$) and $\langle J-H\rangle = 0.74$ ($\sigma = 0.06$), and average redshift $\langle z\rangle = 0.030$ ($\sigma = 0.012$). These average colors correspond to a model located at $z = 0.05$ and age 3 Gyr. This sample shows a larger scatter in the color-color diagram. Most of these galaxies are nearby galaxies (from the PGC and NGC catalogs), and some are galaxies from DC clusters (Caldwell & Rose 1997). All have secure Hubble types, and most of them have known photometric properties in the optical (for B and R total magnitudes; see Table 2). The majority of these galaxies are well matched by the colors provided by the spectrophotometric models for ages representative of early-type galaxies. These galaxies have large apparent radii, and therefore their photometry is more sensitive to color gradients. This is not a problem for more distant galaxies because of the poorer spatial resolution.

Now we compare color properties of samples 1 (field E+A galaxies from the LCRS) and 2 (cluster E+A

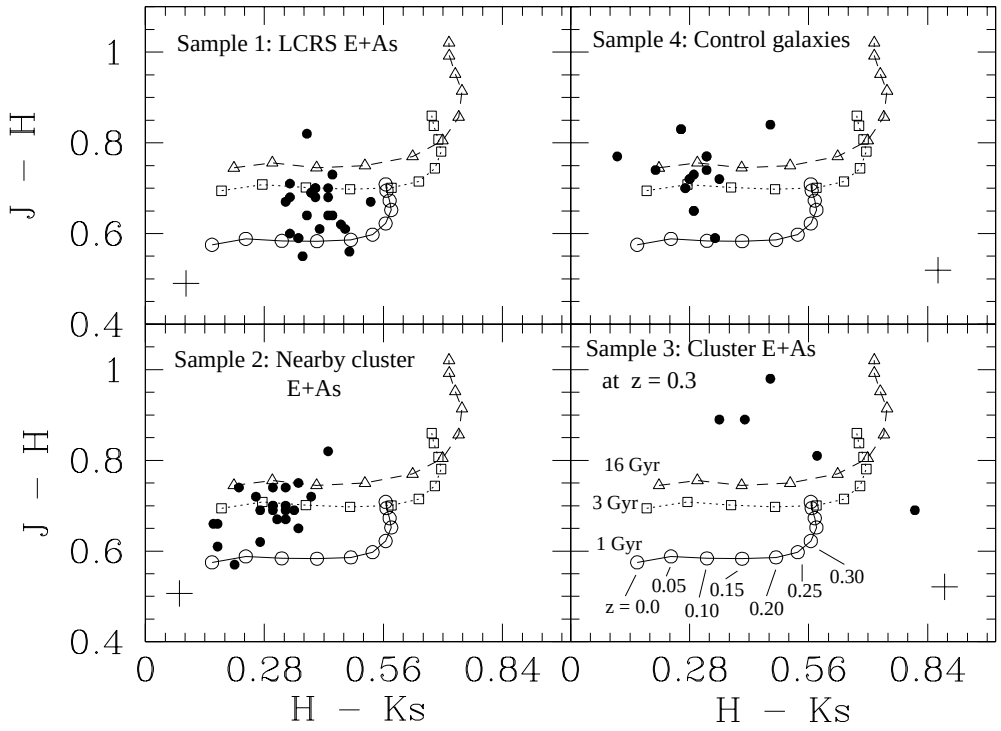

FIG. 7.—Observed colors of the E+A galaxies reported in this paper (*filled circles*) compared with spectrophotometric models of galaxy evolution (*open symbols*). Each panel corresponds to a different E+A sample. Lines represent redshift tracks of an instantaneous burst of solar metallicity for age 1 (*circles*), 3 (*squares*), and 16 Gyr (*triangles*) for the redshifts indicated in the bottom right panel. The crosses are the error bars in the colors. See text for explanations.

galaxies). From Figure 7, it is apparent that sample 1 has the same average $\langle J-H\rangle$ (with a difference of 0.03) but a redder $\langle H-K_s\rangle$ than sample 2 (see above). The difference of 0.12 mag is 2.4 σ and $\sim$1.7 σ away from the intrinsic dispersion of sample 1 and sample 2, respectively. The expected color difference due to K-corrections between $\langle z\rangle = 0.09$ (sample 1) and $\langle z\rangle = 0.046$ (sample 2) is $\sim$0.06 mag for a 2 Gyr model (half of the 0.12 color difference between the two samples), which fits the average colors of both samples 1 and 2 better. Therefore, we can conclude with only a $\sim$1.5 σ confidence level that E+A galaxies from the field are redder than cluster E+A galaxies. The fact that dust extinction is much more significant in $J-H$ than in $H-K_s$ suggests that the color difference observed in $H-K_s$ between sample 1 and sample 2 is not due to differential internal dust extinction. However, because of the observed color dispersion, we cannot give a robust answer supporting stellar population differences instead of internal reddening differences due to extinction. We stress that our differences are at only the 1.5 σ significance level. It is worth noting that $J-H$ color would redden *systematically* by $\sim$0.03–0.05 if we account for foreground or internal extinction (see § 5.3). This would make ages inferred from colors (see Fig. 7) slightly older (0.5 to 1 Gyr) but, in any case, not alter the results of the analysis, since changes are the same for all the galaxy samples.

7. FURTHER ANALYSIS AND DISCUSSION

7.1. *Photometric Uncertainties*

To interpret correctly the color properties of the observed galaxy sample, it is important to keep in mind the sources of uncertainty that affect the colors. The first source of uncertainty is of course the data acquisition itself. Given the nature of the near-IR imaging, the thermal variation of the sky affects the photometry for the faint objects, which require longer integration time, than the brighter ones, sometimes much longer than the typical time of the sky fluctuations (see Fig. 1). However, the nature of these variations is well understood, and the fact that the sky fluctuations are sampled in *real time* and subtracted for each image can reduce this error to 5% (see § 3). The second important source of errors is the procedure employed to compute the magnitude. It is well known that total magnitudes depend on the cut level where the light contribution is null or not significant. In our case, SExtractor computes total magnitudes, integrating all the light up to a given threshold above the sky (typically 1.5 σ) and fitting elliptical isophotes to the profiles. An elliptical aperture for a given galaxy, defined by the elongation ϵ and position angle θ, is computed from the second-order moment in the light distribution, above the isophotal threshold. The "first moment" r_1 is then computed[6] within an aperture twice as large as the isophotal aperture to reach the light distribution in the wings. This approach is very similar to the approach of Kron (1980). The parameter r_1 is then used to define the adaptive aperture for which the total magnitude will be computed. The main axes of the ellipse are defined as $\epsilon k r_1$ and $k r_1/\epsilon$, where k is a value to be fixed by the user. We carried out some tests with both faint and bright galaxies and found that the value $k = 2.5$ allows us to include 90% to 95% of the total flux without introducing additional noise in the aperture. Further details can be found in Arnouts (1996).

[6] The variable r_1 is defined as $r_1 = \sum_r rI(r)/\sum_r I(r)$.

This procedure ensures that not more than 5% of the light is lost.

Another source of uncertainty is the photometric error due to the transformation of the instrumental magnitudes to calibrated magnitudes. This process is well understood, and in general the scatter is small. The errors of the zero points are $\sim 2\%$ to $\sim 7\%$.

The largest uncertainties (now for rest-frame colors) are due to the K-corrections. These uncertainties, as shown in § 5.3, can be very large for galaxies with $z \gtrsim 0.25$, where the change in magnitude produced by the computation of K-corrections, assuming one or another SED, can reach differences as large as 30%, propagating these differences to the rest-frame colors (see Fig. 8). For galaxies with $z \lesssim 0.2$, differences are smaller: $\sim 10\%$ for $0.15 \lesssim z \lesssim 0.2$ and $\sim 5\%$ for $0 \leq z \lesssim 0.15$. To compute reliable $0.15 \lesssim z \lesssim 0.2$ K-corrections, it is fundamental to obtain calibrated spectra at 9000 Å $\lesssim \lambda \lesssim$ 25000 Å for different spectral types, including E+A galaxies. Of course, the nature of the uncertainties lies in the fact that K-corrections are expressed in terms of the morphological type instead of the spectral type. The morphological type relies on a subjective classification procedure, often dependent on the passband (more or less sensitive to the star population that delineates the galaxy morphology) through which the images are obtained, and is always strongly dependent on the image quality. On the other hand, there is no unique and reliable relationship between the spectral type and the morphological type of the galaxies. Even though this is approximately true for normal Hubble types (Folkes, Lahav, & Maddox 1996; Galaz & de Lapparent 1998), the dispersion can be large for some spectral types or active galaxies (Sodré & Stasińska 1999), leading to large uncertainties in the K-correction $= f(z, T\text{-type})$. However, we note that, independently of which spectrophotometric models are used in obtaining rest-frame colors, the K-corrections in the K (or K_s) band are only *weakly* dependent on the spectral type for $z \lesssim 0.2$ (see Figs. 3–5).

7.2. *Implications from Near-IR Colors*

We now examine some color properties of the E+A galaxies observed in the near-IR, keeping in mind the limitations of the accuracy of our photometry, as discussed above. Studying the position of the E+A galaxies in the $(H-K_s, J-H)$-plane shown in Figure 7, we see that *field* galaxies located at $\langle z \rangle \sim 0.09$ (sample 1) have an average $J-H$ color similar to that of E+A galaxies located in nearby clusters ($\langle z \rangle \sim 0.05$, sample 2) but are slightly *redder* in the average $H-K_s$ color (see preceding section). The fact that the color difference of 0.12 mag is significant only at the ~ 1.5 σ level prevents us from proposing a robust conclusion. However, we can now ask how the K-corrections can change this result. Here we examine the answer to this question using the two sets of K-corrections discussed in § 5.3, the PEGASE and the Poggianti K-corrections.

Figure 8 shows average rest-frame colors for our sample of galaxies computed using both sets of K-corrections. Also shown are the colors of the sample of elliptical galaxies from Silva & Bothun (1998). We show the average colors for the cluster and the field galaxies separately. This figure demonstrates that, although the color differences are small, the same trend is observed for each set of K-corrections used. The color difference in $\langle H-K_s \rangle$ between field and cluster

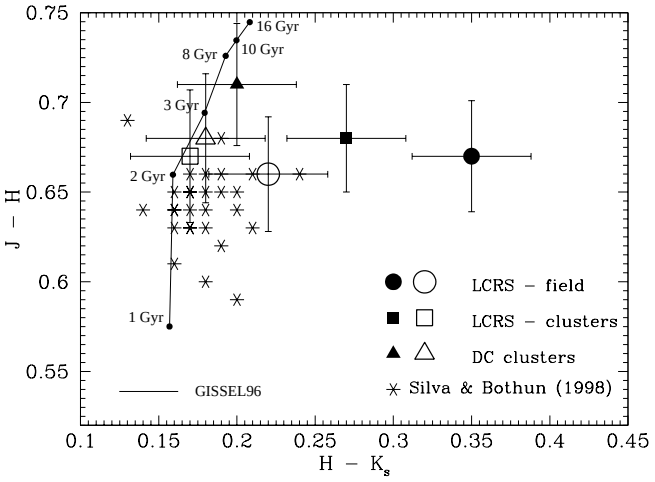

FIG. 8.—Averaged rest-frame colors of E+A galaxies lying in different environments. The LCRS symbols correspond to the 21 E+A galaxies from the sample of Zabludoff et al. (1996). Most of these galaxies are located in the field (at $\langle z \rangle \sim 0.1$), but three of them lie in clusters. The DC cluster E+A galaxies correspond to the E+A galaxies from the sample of Caldwell & Rose (1997), and all of them are located in clusters with $\langle z \rangle \sim 0.05$. Filled symbols indicate that rest-frame colors have been obtained using the Poggianti (1997) K-corrections. Open symbols indicate that averaged rest-frame colors have been obtained using the PEGASE (Fioc & Rocca-Volmerange 1997) K-corrections. *Asterisks*, elliptical galaxies observed by Silva & Bothun (1998); *solid line*, colors of a GISSEL96 (Charlot et al. 1996) instantaneous burst of solar metallicity at $z = 0$ for different ages (*filled circles*). See text for details.

E+A galaxies is about 0.04 mag using PEGASE K-corrections and 0.15 mag using Poggianti K-corrections. Note that in Figure 8 we compare cluster-field colors also for the LCRS sample (three LCRS E+A galaxies belong to clusters). The field E+A galaxies from LCRS are also redder in $\langle H-K_s \rangle$ than the LCRS cluster E+A galaxies are.

As demonstrated by Persson et al. (1983), stellar populations containing a large fraction of AGB stars (1 to 3 Gyr old), have redder $H-K$ color (but similar $J-H$ index), compared with populations that lack such stars. This might suggest that the E+A galaxies in the field have a larger fraction of AGB stars than those in clusters. We emphasize that, although the difference given by the K-correction between $z \sim 0.1$ and $z \sim 0.05$ for samples 1 and 2, respectively, does change the corresponding average colors, the observed color trend for field or cluster does not change.

Note that three of 21 LCRS E+A galaxies are embedded in clusters (LCRS 4, 11, and 20). These galaxies have an average color $\langle H-K_s \rangle = 0.160 \pm 0.041$ using the PEGASE K-corrections, and $\langle H-K_s \rangle = 0.260 \pm 0.005$ using the Poggianti K-corrections. These values are 35% and 22% bluer, respectively, than the average $H-K_s$ color for the LCRS E+A galaxies located in the field and are consistent with the comparison field or cluster between samples 1 and 2.

Galaxies in more distant clusters (sample 3) appear redder in $J-H$ (at 2 σ significance level) than those at lower redshift (compared with both samples 1 and 2). As discussed above, although for this sample K-corrections are critical, the $J-H$ color does not change if one uses a different set of K-corrections. This could be interpreted as a temperature change of the first-ascent giant branch in the stellar populations of these $z \sim 0.3$ E+A galaxies (see Charlot et al. 1996). A further spectroscopic analysis in the near-IR would

settle this question and will also help to clarify possible significant extinction in the J band.

One can also compare the integrated rest-frame colors between the E+A galaxies from sample 2 with the control galaxies that *also* belong to these nearby clusters (e.g., galaxies 52, 53, 59, 60, and 61 in Table 2. We note that the average $H-K_s$ color for both sets of galaxies is similar, and therefore any difference (in the mean) is observed between E+A galaxies and elliptical galaxies belonging to the same cluster. This is not the case if one compares the colors in samples 1 and 2, as shown before. We emphasize that the average $J-H$ color of the E+A galaxies of samples 1 and 2 is similar to the average $J-H$ of the control sample (at the 1 σ significance level; see Fig. 7).

It is worth noting that all the K-corrections used to obtain average rest-frame colors, as shown in Figure 8, have been computed using solar-metallicity models, assuming that K-corrections for a given IMF, age, and star formation rate (SFR) scenario do not depend strongly on metallicity. We tested this assumption using GISSEL96 SEDs with different metallicities. Several tests were carried out for different ages, IMFs, and SFRs, and metallicities between the extreme values of [Fe/H] $= -1.65$ and [Fe/H] $= +1.00$. Differences in K-corrections between these two extreme metal-poor and metal-rich models can be as high as 0.3 mag in J at $z = 0.3$ for a large range of fundamental parameters (age, IMF, and SFR). For more modest metallicity differences (probably more realistic) between models, variations in K-corrections, for the different near-IR photometric bands, are between 0.15 mag for J and 0.05 mag for H and K_s, at $z = 0.3$. For smaller redshifts, these differences are even smaller. Figure 9 shows K-correction differences in near-IR bands as a function of redshift for two SEDs with different metallicities ([Fe/H] $= -0.30$ and [Fe/H] $= +0.1$, shown in inset of figure), derived from instantaneous bursts with the same age and IMF (in both cases Scalo IMF). These K-corrections differences imply $J-H$ and $H-K_s$ colors shifts no larger than 0.08 mag up to $z \sim 0.3$, given that differences in K-corrections due to different metallicity have the same sign. We conclude that for a typical interval of metallicity found in the field and in clusters the effect of varying metallicity should not be significant on the K-correction uncertainties or, hence, on rest-frame colors. However, for more accurate estimates of near-IR colors from broadband photometry, especially at higher redshift ($z \gtrsim 0.5$), metallicity does play a significant role on the K-corrections.

8. SUMMARY AND CONCLUSIONS

The E+A galaxies reported here include 32 galaxies from clusters and 18 galaxies from the field. In addition, 13 nearby galaxies that do not present poststarburst activity were observed (five located in clusters at $z \sim 0.05$ and eight located in the field at very low redshift). All the galaxies have been observed in the near-IR bands J, H, and K_s during photometric nights at Las Campanas Observatory. Total apparent magnitudes and colors were derived. The $(H-K_s, J-H)$ color-color diagram of the observed galaxies is compared with the expected corresponding colors of spectrophotometric models of galaxy evolution at different redshifts. The models are those generated by GISSEL96 (Charlot et al. 1996). There is overall agreement between these expected colors and the observed ones for the E+A galaxies located in nearby clusters ($\langle z \rangle \sim 0.05$) and for E+A galaxies located in the field ($\langle z \rangle \sim 0.1$). The comparison of the colors of these two samples shows that even though cluster E+A galaxies appear bluer than field E+A galaxies, the color difference is significant only at the $\sim 1.5\,\sigma$ level, and therefore we cannot strongly affirm that stellar

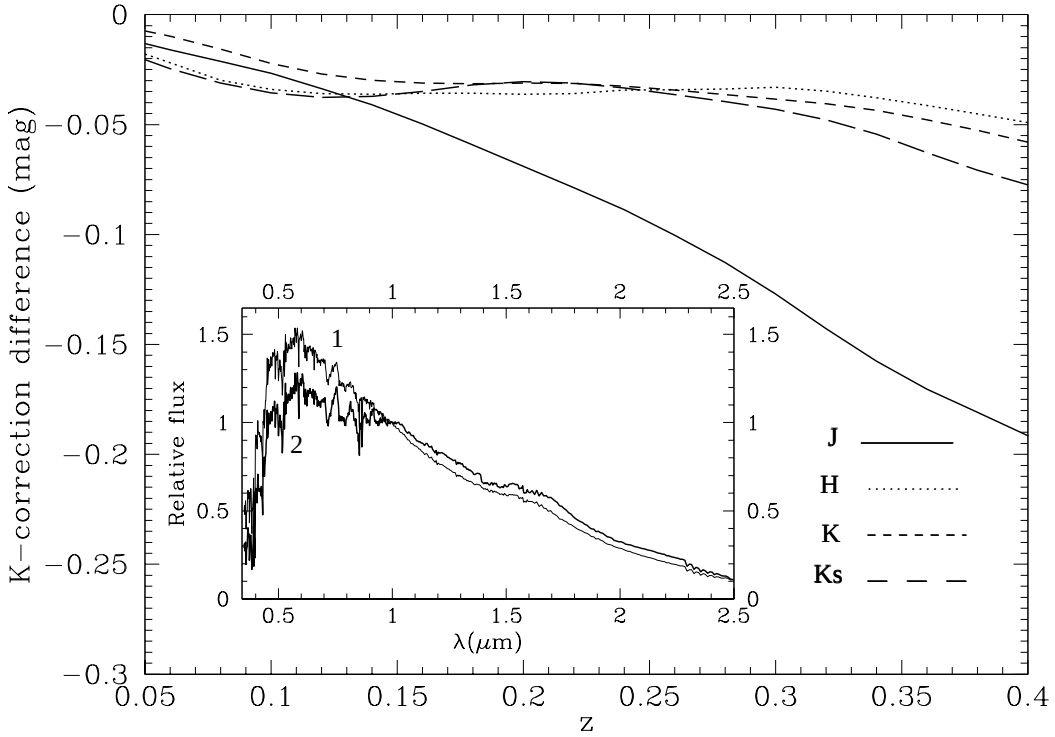

FIG. 9.—K-correction differences in J, H, K, and K_s as a function of redshift for two SEDs having different metallicity. *Inset*: Two SEDs are simple instantaneous bursts with a Scalo initial mass function (Scalo 1986) and an age of 10 Gyr. Differences in K-corrections are expressed as the difference between the K-correction for SED 1 ([Fe/H] $= -0.30$) and the K-correction for SED 2 ([Fe/H] $= +0.10$).

population differences are observed between these two populations.

The colors of the E+A galaxies located in more distant clusters with $z = 0.3$, on the other hand, do not agree with the color expected from models. In the mean, they appear bluer than expected in $H-K_s$ (by ~ 0.3 mag) and redder in $J-H$ (by ~ 0.15 mag). The possible interpretation of this failure is strong internal reddening (mostly in the J band), not considered in models.

To derive a more complete comparison with models, rest-frame colors were also obtained using two different sources of K-corrections: one based on the work of Poggianti (1997) and the other computed using the spectrophotometric model PEGASE (Fioc & Rocca-Volmerange 1997). We have shown that such K-corrections can be significant for $z \sim 0.2$ in the K bands (or any band centered at 2 μm), although they are not a strong function of spectral type. In addition, large differences exist in the K-corrections between these two models, having a large impact on the derived quantities, such as rest-frame colors for high-redshift galaxies. We have compared average rest-frame colors of E+A galaxies located in the field and in clusters. Results show that average rest-frame near-IR colors of E+A galaxies located in clusters at $z \sim 0.05$ (Caldwell & Rose 1997) and field E+A galaxies located at $z \sim 0.1$ (from the LCRS; Zabludoff et al. 1996) follow the same color trend in $J-H$ and $H-K_s$ observed in the comoving color-color diagram: E+A galaxies located in nearby clusters appear bluer than field E+A galaxies ($z \sim 0.1$).

As for comparing the observed colors with the GISSEL96 colors at different redshifts, the models do not fit the rest-frame colors of the E+A galaxies observed in clusters at $z \sim 0.3$ as well. Their $H-K_s$ colors appear bluer (using the K-corrections of PEGASE) or redder (using the K-corrections of Poggianti) compared with the models. Their $J-H$ color index, although not particularly sensitive to one or the other K-correction, is also redder than the colors predicted by the models. The color of the control galaxies, most of them ellipticals at $z \lesssim 0.01$ and the others from clusters at $z \sim 0.05$, agree with the near-IR colors predicted by models.

Integrated colors between the *field* E+A galaxies and the *cluster* E+A galaxies of the LCRS (LCRS 4, 11, and 20; see Table 2) are similar, although those in clusters seem to be slightly ($\sim 25\%$) bluer in $H-K_s$ than the average color. This result is the same for both sets of rest-frame colors, the set corrected by the PEGASE K-corrections and the set corrected by the Poggianti K-corrections (see Fig. 8). On the other hand, the corresponding $J-H$ color is similar for the cluster and field E+A galaxies in sample 1.

To build more robust results, more field and cluster E+A galaxies have to be observed between $z = 0.1$ and $z = 1.0$. Spectroscopic observations of normal and E+A galaxies at different redshifts in the near-IR are necessary (1) to obtain calibrated SEDs and realistic K-corrections and (2) to compare the spectra of the E+A galaxies with those of normal galaxies in the whole spectral range 3500 Å $\lesssim \lambda \lesssim$ 25000 Å. We expect to continue this research by imaging new E+A galaxies in the near-IR at higher redshift, as well as obtaining near-IR spectra to construct a useful and larger database of normal and poststarburst galaxies in a large spectral range. To increase the number of E+A galaxies, some field galaxies already classified as E+A galaxies are being observed in the near-IR at Las Campanas. Some of these galaxies belong to the ESO Sculptor Survey (de Lapparent et al. 1997), and results will be published soon. Other wide-field surveys will provide a wealth of data for E+A galaxies at $0.01 \lesssim z \lesssim 0.2$, such as Sloan (Loveday & Pier 1998), Fan et al. (1998), and the 2dF survey (Colless 1998), whose data are expected to become available to the public. In a forthcoming paper, we shall investigate systematic properties on the surface photometry and colors of the E+A galaxies.

I thank Ron Marzke, Eric Persson, and Ann Zabludoff for fruitful discussions on the nature of the E+A galaxies. I acknowledge Mauro Giavalisco for his help with the DIMSUM software. I also acknowledge Mario Hamuy, René Méndez, Mark Phillips, Miguel Roth, and Bill Kunkel in helping to improve the preliminary version of this paper. It is a pleasure to thank all the staff at Las Campanas Observatory. The author would like to thank the anonymous referee for useful comments and suggestions. This research has made use of the NASA IPAC Extragalactic Database (NED), which is operated by the Jet Propulsion Laboratory, California Institute of Technology, under contract with the National Aeronautics and Space Administration. This work is made possible through fellowship C-12927, under agreement between Fundación Andes and the Carnegie Institution of Washington.

REFERENCES

Arnouts, S. 1996, Ph.D. thesis, Univ. Paris VII
Bershady, M. 1995, AJ, 109, 87
Bertin, E., & Arnouts, S. 1996, A&AS, 117, 393
Bower, R., Lucey, J., & Ellis, R. 1992a, MNRAS, 254, 589
———. 1992b, MNRAS, 254, 601
Bruzual, A. G., & Charlot, S. 1993, ApJ, 405, 538
Butcher, H., & Oemler, A. 1978, ApJ, 219, 18
Caldwell, N., & Rose, J. 1997, AJ, 113, 492
Cardelli, J., Clayton, G., & Mathis, J. 1989, ApJ, 345, 245
Charlot, S., Worthey, G., & Bressan, A. 1996, ApJ, 457, 625
Colless, M. 1998, in Wide Field Surveys in Cosmology, ed. S. Columbi, Y. Mellier, & B. Raban (Paris: Ed. Frontières), 77
Couch, W., & Sharples, R. 1987, MNRAS, 229, 423
de Lapparent, V., Galaz, G., Arnouts, S., Bardelli, S., & Ramella, M. 1997, Messenger, 89, 21
de Vaucouleurs, G., de Vaucouleurs, A., & Corwin, H. 1976, Second Reference Catalogue of Bright Galaxies (Austin: Univ. Texas Press)
de Vaucouleurs, G., de Vaucouleurs, A., Corwin, H., Buta, R., Paturel, G., & Fouqué, P. 1991, Third Reference Catalogue of Bright Galaxies (Berlin: Springer)
Dressler, A., & Gunn, J. 1983, ApJ, 270, 7
Edmunds, M. G. 1992, in The Stellar Populations of Galaxies, ed. B. Barbuy & A. Renzini (Dordrecht: Kluwer), 277
Fabricant, D., McClintock, J., & Bautz, M. 1991, ApJ, 381, 33
Fairall, A., et al. 1992, AJ, 103, 11
Fan, X., et al. 1998, BAAS, 193, No. 02.05
Ferreras, I., Charlot, S., & Silk, J. 1999, ApJ, 521, 81
Fioc, M., & Rocca-Volmerange, B. 1997, A&A, 326, 950
Folkes, S., Lahav, O., & Maddox, S. 1996, MNRAS, 283, 651
Franx, M. 1993, ApJ, 407, L5
Frogel, J., Persson, E., Matthews, K., & Aaronson, M. 1978, ApJ, 220, 75
Galaz, G., & de Lapparent, V. 1998, A&A, 332, 459
Kennicutt, R. 1992, ApJS, 79, 255
Kron, R. 1980, ApJS, 43, 305
Liu, C., & Green, R. 1996, ApJ, 468, L63
Loveday, J. 1996, MNRAS, 278, 1025
Loveday, J., & Pier, J. 1998, in 14th IAP meeting, Wide Field Surveys in Cosmology (Paris: Ed. Frontières), 317
Oke, J., & Sandage, A. 1968, ApJ, 154, 21
Persson, E., Cohen, J., Matthews, K., Frogel, J., & Aaronson, M. 1983, ApJ, 266, 105
Persson, E., Frogel, J., & Aaronson, M. 1979, ApJS, 39, 61
Persson, E., Murphy, D., Krzeminski, W., Roth, M., & Rieke, M. 1998, ApJ, 116, 2475
Poggianti, B. 1997, A&AS, 122, 399
Prugniel, P., & Hérédeau, P. 1998, A&AS, 128, 299

Rakos, K., & Schombert, J. 1995, ApJ, 439, 47
Ronen, S., Aragón-Salamanca, A., & Lahav, O. 1999, MNRAS, 303, 284
Scalo, J. 1986, Fundam. Cosmic Phys., 11, 1
Schlegel, D., Finkbeiner, P., & Davis, M. 1998, ApJ, 500, 525
Shectman, S., Landy, S., Oemler, A., Tucker, D., Lin, H., Kirshner, R., & Schechter, P. 1996, ApJ, 470, 172
Silva, D., & Bothun, G. 1998, AJ, 116, 85
Sodré, L., & Stasińska, G. 1999, preprint (astro-ph/9903130)
Spellman, K., Madore, B., & Helou, G. 1989, PASP, 101, 360
Wise, M., & Silva, D. 1996, ApJ, 461, 155
Worthey, G. 1994, ApJS, 95, 107
Zabludoff, A., Zaritsky, D., Lin, H., Tucker, D., Hashimoto, Y., Shectman, S., Oemler, A., & Kirshner, R. 1996, ApJ, 466, 104